PHYSICAL REVIEW E **110**, 024606 (2024)

Mechanical testing of colloidal solids with millipascal stress and single-particle strain resolution

J. Zsolt Terdik [*]
John A. Paulson School of Engineering and Applied Sciences, Harvard University, Cambridge, Massachusetts 02138, USA

David A. Weitz
John A. Paulson School of Engineering and Applied Sciences, Harvard University, Cambridge, Massachusetts 02138, USA;
Department of Physics, Harvard University, Cambridge, Massachusetts 02138, USA;
and Wyss Institute for Biologically Inspired Engineering, Harvard University, Boston, Massachusetts 02115

Frans Spaepen
John A. Paulson School of Engineering and Applied Sciences, Harvard University, Cambridge, Massachusetts 02138, USA

(Received 4 January 2024; revised 20 May 2024; accepted 8 July 2024; published 20 August 2024)

We introduce a technique, traction rheoscopy, to carry out mechanical testing of colloidal solids. A confocal microscope is used to directly measure stress and strain during externally applied deformation. The stress is measured, with single-mPa resolution, by determining the strain in a compliant polymer gel in mechanical contact with the colloidal solid. Simultaneously, the confocal microscope is used to measure structural change in the colloidal solid with single particle resolution during the deformation. To demonstrate the utility and sensitivity of this technique, we deform a hard-sphere colloidal glass in simple shear, and from the macroscopic shear strain and measured stress determine the stress-strain curve. Using the stress-strain curve and measured shear modulus, we decompose the macroscopic shear strain into an elastic and a plastic component. We also determine a local strain tensor for each particle using the changes in its nearest-neighbor distances. These local strains are spatially heterogeneous throughout the sample, but, when averaged, match the macroscopic strain. A microscopic yield criterion is used to split the local strains into subyield and yielded partitions; averages over these partitions complement the macroscopic elastic-plastic decomposition obtained from the stress-strain curve. By combining mechanical testing with single-particle structural measurements, traction rheoscopy is a unique tool for the study of deformation mechanisms in a diverse range of soft materials.

DOI: 10.1103/PhysRevE.110.024606

I. INTRODUCTION

Confocal visualization of colloidal solids has provided valuable insight into the internal deformation of soft materials. Due to diffusive time and micron size of colloidal particles, these internal deformations can be resolved and tracked, down to the individual particle [1–4]. As a result, microscopic deformation mechanisms such as dislocation motion in crystals, gel strand deformation in gels, and shear transformation zones in glasses can be directly visualized at the smallest material length scales in three dimensions using a commercial confocal microscope. The micron size of individual colloidal particles enables visualizing these deformation mechanisms at single-particle resolution, but necessarily gives rise to compliant solid phases [5]. Due to the compliance, small shear stresses, on the scale of single mPa, are sufficiently strong to activate the heterogeneous deformation mechanisms that govern the material response under external deformation. The measurement of these small stresses and their coupling to microscopic deformation mechanisms is the central challenge in combining rheology of colloidal solids with confocal microscopy visualization of the microscopic deformation.

In this paper we introduce a technique, traction rheoscopy, to measure shear stresses with mPa resolution, while simultaneously resolving internal strain with single-particle resolution in colloidal solids undergoing deformation. To demonstrate the utility of traction rheoscopy, we study a hard-sphere colloidal glass under simple shear deformation and resolve local strain heterogeneities that occur as the macroscopic material response undergoes an elastic-plastic transition.

II. EXPERIMENTAL DESIGN

In traction rheoscopy a colloidal solid is placed into mechanical contact with a calibrated elastic substrate to form a bilayer which is then deformed in simple shear. When the bilayer is deformed the shear strains in the colloidal solid, γ_{xz}, and calibrated elastic substrate, $\tilde{\gamma}_{xz}$, depend on their respective shear moduli, G and $\tilde{G}$, as shown schematically in Fig. 1. Due to a no-slip boundary condition between the colloidal solid and calibrated substrate, the shear stress σ_{xz} is constant across the bilayer. Confocal microscopy is used to track the displacements of individual fluorescent tracer particles embedded in the calibrated substrate and determine its shear strain, $\tilde{\gamma}_{xz}$. This deformation of the substrate is combined with its calibrated modulus, $\tilde{G}$, to determine the stress in the

---

[*] Contact author: terdik@g.harvard.edu

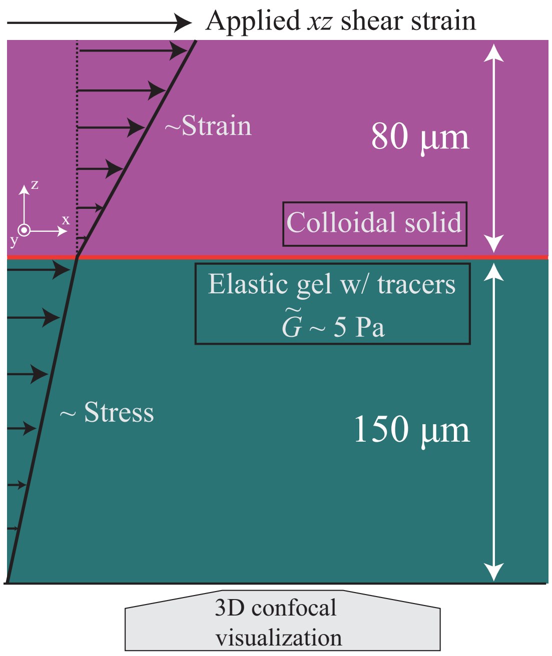

FIG. 1. Traction rheoscopy. A bilayer of colloidal solid (magenta) in mechanical contact with calibrated silicone gel (green) is deformed under simple shear. The thick, compliant gels, and the high strain resolution afforded by particle tracking, make it possible to determine the average stress across the bilayer with mPa resolution. The height-dependent deformation profile is depicted schematically with black arrows, and measured experimentally by tracking the displacements of tracer particles dispersed in the gel and of the densely packed particles that make up the colloidal solid.

bilayer $\sigma_{xz} = \tilde{G}\tilde{\gamma}_{xz}$. Independent of the stress measurement, the strain in the colloid solid, γ_{xz}, is measured with single-particle resolution by tracking the positions of $\sim 5 \times 10^5$ individual, densely packed colloidal particles that make up the colloidal glass, as shown in Fig. 2.

Based on this experimental design, a back-of-the-envelope estimate of the stress resolution shows that mPa stresses can be directly measured with confocal microscopy provided that the calibrated substrate is sufficiently thick and compliant. The stress resolution, $\delta\sigma_{xz}$, determines the lower limit on the magnitude of measurable stress. It is limited by the smallest resolvable shear strain, $\delta\tilde{\gamma}_{xz}$, which is scaled by $\tilde{G}$.

Confocal microscopy and single-particle locating of thick substrates, $\tilde{h} \approx 150$ µm, enable high strain resolution:

$$\delta\tilde{\gamma}_{xz} = \frac{\delta x}{\tilde{h}} = \frac{25\ \text{nm}}{150\ \mu\text{m}} = 1.7 \times 10^{-4}, \tag{1}$$

where the minimum resolvable displacement, δx, is limited by the resolution of single-particle locating, and the thickness, $\tilde{h}$, is determined by sample preparation protocols. For substrates with compliant moduli of $\tilde{G} \sim 1$ Pa, shear stresses below 1 mPa can be resolved:

$$\delta\sigma_{xz} = \tilde{G}\,\delta\tilde{\gamma}_{xz} < 1\ \text{mPa}. \tag{2}$$

In addition to the stress measurement, imaging through the transparent substrate using confocal microscopy enables independent measurements of the internal deformation of the colloidal solid from the displacements of the individual particles that make up the solid.

Experimentally achieving the combined stress and strain resolution poses three central challenges. First, traction rheoscopy relies on confocal imaging of a bilayer, with thickness greater than 100 µm, composed of heterogeneous components, including a polymer gel, embedded tracers, and the densely packed colloidal solid. Consequently, optical index matching of these components is essential to maintain locating resolution. Second, the elastic substrate must be highly compliant, which presents challenges to shaping the material and forming a bilayer geometry. Third, to resolve the build-up of strain during plastic deformation, the cumulative deformation is spread over hundreds of confocal imaging stacks to ensure that the displacements between frames are small and that individual particles can be tracked. As a result, the fine strain resolution over large cumulative strains necessitates hours of continuous imaging resulting in several terabytes of image data to be analyzed per experiment.

Comparison to commercial rheometers

Commercial rotational rheometers can also routinely measure small, mPa stress relevant for soft materials. The stress resolution is achieved by transducing local tractions into local torques and then integrating across the tool geometry. A typical tool geometry consisting of a parallel plate of radius R produces a total torque M:

$$M = \int_0^R 2\pi r(\sigma r)\, dr. \tag{3}$$

For a uniform distribution of shear stress of magnitude $\sigma = 1$ mPa, the total total torque measured on a parallel plate of 50 mm diameter is

$$M = 2\pi\sigma \int_0^R r^2\, dr = 2\pi\sigma \frac{r^3}{3}\bigg|_0^{R=25\ \text{mm}} = 33\ \text{nN m},$$

at least two orders of magnitude larger than the minimum torque limit of commercial rheometers $M^*_{\text{rheo}} = 0.3$ nN m.

Unlike commercial rheometers, however, traction rheoscopy achieves a mPa stress resolution by increasing the compliance of the stress transducer without integrating over areas larger than microscopy field of view. To compare the stress resolution of traction rheoscopy with that of commercial rheometers, consider a tool geometry consisting of a small plate with area A held at a fixed radial distance R. In this geometry, the torque measured by the rheometer is amplified by the lever arm R, but spatial integration is limited to the area A.

A uniform shear stress of $\sigma = 1$ mPa integrated over an area comparable to microscopy field of view obtained using traction rheoscopy, $A = (250\ \mu\text{m}) \times (250\ \mu\text{m})$, produces a total shear force $F = 62.5$ pN. Transducing this force into a measurable large torque $M > M^*_{\text{rheo}}$ entails an impractically long lever arm R:

$$R = \frac{M^*_{\text{rheo}}}{F} = \frac{0.3\ \text{nN m}}{62.5\ \text{pN}} \geqslant 4.8\ \text{m}.$$

Further restricting the area, $A \sim d^2$, to match the distance between individual tracers in the gel, $d \sim 10$ µm, would be

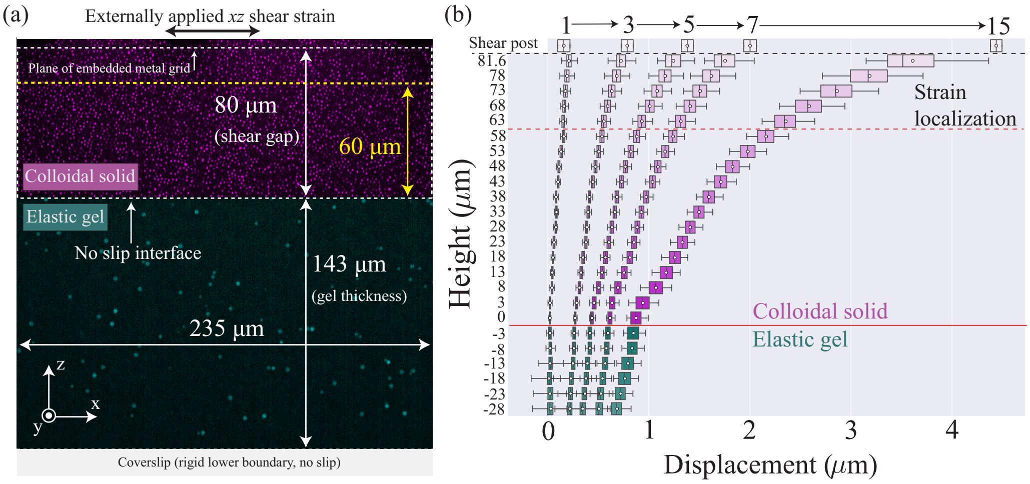

FIG. 2. Independent measurements of stress and strain using traction rheoscopy. (a) Confocal microscopy image of shear geometry used in traction rheoscopy. A colloidal glass (upper, false-color magenta) is formed atop a silicone gel with embedded tracers (lower, false-color cyan). A cross-sectional slice with normal in the y direction is shown with annotations of the geometry. (b) Experimental data of particle displacements in the shear direction as a function of height for a selection of imaging frames (top row) during loading. The interface between the silicone gel and colloidal solid is shown with a solid red line at height zero and is shown schematically (a). The positions of the colloidal particles (magenta, upper) and tracers in the silicone gel (cyan, lower) are binned as function of height relative to the interface. For each height, the mean (central dot), interquartile range (box), and middle 90% (whiskers) are shown. The displacement curves show pronounced bending at heights above 60 μm as indicated by the dashed line. The left and right edges of the uppermost bin, labeled shear post, correspond to the position of the shear post at the start and end of the frame acquisition.

analogous to the stress measured in traction rheoscopy from individual tracer particles in the gel; 1 mPa of stress distributed across this even smaller area would require a lever arm of $R \geqslant 3000$ m to achieve a measurably large torque on a commercial rheometer.

Related techniques have combined confocal microscopy with shear cells or commercial rheometers for stress measurements [6–10]. Unlike these hybrid instruments, the shear cell used in traction rheoscopy can be mounted and easily unmounted on any inverted confocal microscope. Recently, boundary stress microscopy has combined confocal microscopy, a commercial rheometer, and traction force microscopy to determine spatially dependent stresses, on the order of ~1 Pa, in sheared collagen networks [11] and shear thickening colloidal suspensions [12]. While both traction rheoscopy and boundary stress microscopy use the deformation of a calibrated elastic substrate to measure stress during externally imposed deformation, the stresses measured with traction rheoscopy are three orders of magnitude smaller.

III. OPTICAL INDEX MATCHING OF THE BILAYER

The bilayer design in traction rheoscopy is composed of heterogeneous components that are imaged using a confocal microscope. Due to this heterogeneity, optical index matching *within* each layer—i.e., the gel tracers with the elastic substrate and the colloidal particles with the solvent—is essential to eliminate scattering. Additionally, since the bilayer geometry is ~220 μm thick, confocal imaging through this volume introduces additional optical aberrations, known as spherical aberrations, that are caused by refractive index mismatch between the bilayer and the immersion medium of the objective [13,14]. In order to ensure high-resolution imaging of the particle positions and displacements, both optical scattering and spherical aberrations are minimized by fixing the refractive index of all components to a single target, $n = 1.45$, determined by the immersion medium of the objective [15].

Silicone gel formulation. The silicone gels that serve as the calibrated elastic body were formulated to have a target refractive index and tunable elastic modulus [16]. The silicone gel has a true elastic response characterized by a storage modulus that is much greater than the loss modulus at the low frequencies of the experiment, as shown in Fig. 3.

The gel formulation consists of two parts: materials selection and formulation. The materials selection was based on meeting a hierarchy of constraints: chemical immiscibility with solvents used in the colloid dispersion, compliant modulus, and refractive index matching. Silicones were selected because they are immiscible with the polar solvent formamide, which is the index-matching solvent in the colloid phase [17]. Next, compliant gels near the gelation threshold were formulated by the addition of nonreactive silicone oil to the pre-gel solution [18]. Finally, the refractive index was adjusted to meet the target by using a solution of silicone polymers with variable diphenyl substitutions in place of dimethyl groups along the siloxane backbone. Increasing the diphenyl substitution increases the refractive index from $n = 1.4$ to $n = 1.5$. Based on these constraints, *poly*-diphenyl-*co*-dimethyl siloxane (PDPS) polymers with platinum catalyzed vinyl-hydride addition were selected as the material for the elastic substrates [16]. All polymers and reagents are listed in Table I; they are commercially available and the product codes from Gelest are given parenthetically in the text.

A solution of silicone oils, λ, with the target refractive index is formulated from nonreactive PDPS oils with refractive indices just above and below the target (PDM-1922 and

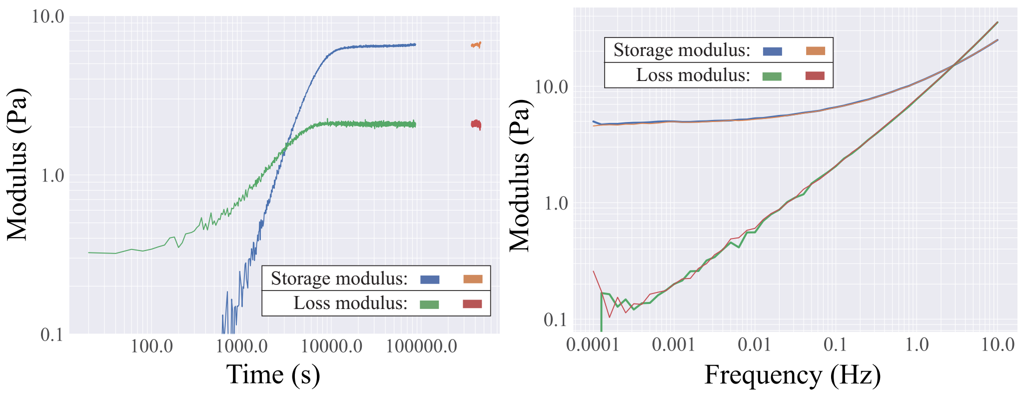

FIG. 3. Calibration of the silicone gel substrate. Time-dependent curing and frequency-dependent storage and loss moduli are calibrated for the silicone gel used in experiment at 25 °C. The storage and loss modulus are measured during the curing process (left panel, blue and green curves, respectively) at fixed frequency and show a plateau after 10^4 s. Then the frequency-dependent moduli are measured (right panel, blue and green curves). The storage modulus at frequencies below 10^{-3} s^{-1} is 4.9 Pa, and the loss modulus is 50 times lower, indicating true elastic solid response at low frequencies. An additional time-dependent curing step shows no change in the moduli (left panel, yellow and red curves). The frequency-dependent storage and loss moduli (yellow and red curves, right panel) show no change in moduli after four days of curing.

PDM-081, respectively). Similarly, high-molecular-weight, vinyl-terminated PDPS polymers with refractive indices above and below the target (PDV-1641 and PDV-0541) were selected. Finally, the hydride functional polymer (HDP-111), which is a minority component and is nearly index matched to the target, was selected as well as a room temperature curing platinum catalyst (SIP 6831.2 LC).

The two vinyl-terminated and hydride-functional polymers were diluted in the refractive index-matching solution to obtain stock solutions b_1, b_2, and c. The mass percent reactive polymer and silicone oil in each of these four stock solutions is given in Table I. These stock solutions along with additional index matching silicone oil, λ, are mixed at a mass ratio of (b_1:b_2:c:λ). For the stock solutions b_1 and b_2, the mass percents of the reactive polymers are set so that when mixed at equal mass ratios, $b_1 = b_2 = b$, and gelled, the cross-linked network is predicted to be index matched to the target. This prediction is based on the average diphenyl substitution of the vinyl-terminated polymers in the stock solutions b_1 and b_2. Using this formulation, the ratio of hydride-to-vinyl functional groups can be easily varied; for the gels used in this work (b:c) = (1:0.7). With this formulation, the shear modulus is controlled by the total silicone oil mass fraction, which can be adjusted near the gel point by the final component λ. Crucially, both the cross-linked network and the silicone oil have a refractive index that matches the target, and hence varying λ adjusts the shear modulus without altering the refractive index away from the target.

TABLE I. Composition of stock solutions. All reagents are from Gelest, and their associated product codes are listed in Component 1 column. A nonreactive liquid filler, λ, is mixed from two silicone oils to meet the target refractive index. The additional stock solutions are reactive components mixed with λ at mass ratios given in column 3.

Stock solution	Component 1	Mass percent component 1	Component 2
λ	PDM-1922	26%	PDM-0821
b_1	PDV-1641	19.8%	λ
b_2	PDV-0541	16.7%	λ
c	HDP-11	1.1%	λ
Catalyst	SIP6831.2LC	10%	λ

Rheological calibration. For this work, the pre-gel solution has composition mass ratios of $(b_1{:}b_2{:}c{:}\lambda) = (1{:}1{:}0.7{:}5.97)$. Once the pre-gel solution is mixed, 10 µl of catalyst solution is added to a 1 g aliquot and loaded onto a strain controlled rheometer. A 50 mm parallel plate is used with a typical gap height of 250 µm. The work time of the pre-gel solution is approximately 20 minutes, and the gel is fully cured at room temperature after 24 hours as shown in Fig. 3. A frequency sweep at 2% applied strain is carried out to calibrate the storage and loss moduli. As shown in Fig. 3, the low-frequency plateau is reached at frequencies $f < 10^{-3}$ Hz; the storage modulus is 4.9 Pa, and loss modulus is 50 times lower, indicative of a true elastic response. A subsequent curing step and frequency sweep shows no change in the mechanical properties after four days.

Particle synthesis. Traction rheoscopy requires synthesis of two sets of colloidal particles that can be dispersed in an index-matching solvent of either formamide or silicone oil. These two solvents are immiscible, but have the same refractive index that also matches the target refractive index. The index match between the particles and either solvent is achieved by using particles composed of a random copolymer of *poly*-trifluoroethyl-*co*-methyl methacrylate (*poly*-MMA-*co*-FEMA) introduced in Ref. [17]. For both sets of particles an identical monomer solution containing 19.594 g of FEMA and 9.395 g of MMA is used during the dispersion polymerization steps. The gel tracers are homogeneously dyed and stabilized by a silicone polymer brush, while the particles in the colloidal solid phase have a fluorescent core, a nonfluorescent shell, and an anionic polyelectrolyte stabilizing brush. To ensure hard sphere interactions between the polyelectrolyte stabilized particles, the final solvent is 30 mM KCl in formamide.

The synthesis of silicone-stabilized tracers is detailed in [16]. The synthesis is a modification of Ref. [19] with a diphenyl-substituted silicone brush and MMA/FEMA as the polymer composition. The synthesis proceeds in two steps: synthesis of a reactive graft copolymer, and dispersion polymerization in which the graft copolymer serves as the stabilizer. The graft copolymer was synthesized by reacting low-molecular-weight, vinyl-terminated PDPS polymers (PDV-0525 and PDV-1625, Gelest) with a solution of methyl methacrylate (MMA) and trifluoroethyl methacrylate (FEMA). This graft copolymer was used as a stabilizer during dispersion polymerization with a monomer solution of MMA/FEMA. After synthesis, the gel tracers are dispersed in an index-matching solution of silicone oils, λ, and residual organic solvent used during particle synthesis is removed by rotatory evaporation.

This stock solution of tracers in silicone oil is substituted for λ in the gel formulation to obtain gels with embedded tracers. The diameter of the tracers is 2–3 μm, which is much larger than the mesh size ξ of the polymer gel estimated from the calibrated modulus: $\xi = (4.1\ \text{pN}\,\text{nm}/4.9\ \text{Pa})^{1/3} \approx 100$ nm. The tracers are dilute, typically 1% by volume; their overall concentration in the pre-gel solution can be adjusted after initial calibration steps by centrifuging the pre-gel solution, removing a portion of the supernatant and redispersing the tracers. Provided that the final tracer concentration remains dilute, the increased concentration of tracer results in only a small increase in the shear modulus [20]. The tracers sediment as the gel cures which can exploited during the curing process to increase their concentration at the top of the gel, where the strain resolution is largest.

The synthesis for polyelectrolyte-stabilized, fluorescent-core/nonfluorescent shell particles of the colloid sample follows Ref. [17], with only minor modifications; the monomer solution of MMA/FEMA is used during dispersion polymerization steps in order to achieve the largest density mismatch between the particles and formamide.

Colloidal glasses, crystals, and gels. The index matching and chemical compatibility constraints of traction rheoscopy limit the choice of materials that can be combined to form a bilayer. In particular, the solvent used to index match the colloid solid phase must be immiscible with the silicone oil that constitutes the majority of the gel phase. Operating within these constraints, the particle synthesis in Ref. [17] can be used to generate a wide range of colloidal solid phases. By altering the size of the particles formed during synthesis and the sedimentation flux during deposition, hard-sphere colloidal crystals, binary colloidal crystals, and binary colloidal glass can be formed. The charge of the stabilizing polyelectrolyte brush can be altered giving rise to attractive glasses or gels, a depletant of *poly*-ethylene glycol can be dispersed in formamide to achieve short range attractive potentials, and the colloid dispersion can be density matched by using a solvent and polymer composition detailed in Ref. [17]. Each of these variations has been tested with the silicone gels.

IV. SUBSTRATE GEOMETRY

Shear cell and sacrificial molds. The preparation of the bilayer geometry required the development of several techniques to mold the compliant silicone gel, to functionalize its surface, and to deposit the colloidal dispersion without forming a contact line or destroying the interface [21]. A small, modular shear cell was developed with components specific to the sample processing steps. This shear cell can be mounted on any inverted confocal microscope used to image the bilayer.

The sample processing techniques in Ref. [21] are used to cast a near-critical silicone gel, formulated in Ref. [16], into a sacrificial sugar-glass mold. The sacrificial mold serves two roles: a *mold* allows casting of uniformly thick substrates independent of wetting and capillary length of the uncured pre-gel solution, while the *sacrificial* feature enables dissolving the mold to expose the top surface of the compliant gel without the formation of an air-liquid-gel contact line that would lead to distortions of the compliant gel [22,23]. Similarly, subsequent sample processing steps are carried out with only partial exchange of the solvent above the gel so as to avoid the formation of contact line. The thickness, $\tilde{h} = 145$ μm, is set by an adhesive spacer placed between the cover glass and the sacrificial sugar-glass mold. Crucially the gel layer is thick enough to allow single mPa stress resolution, as shown in Eqn. (1) and (2), but thin enough to be scanned through with only a portion of the free-working distance of the objective.

Formation of the bilayer. Once the sacrificial capillary is created and a stock of pre-gel solution has been formulated and adjusted to attain the target modulus, an 1 g aliquot is used to form the gel substrate and carry out a final calibration. From the aliquot, drops are used for capillary loading of the sample cell, which is completed in a few minutes, while the remainder is loaded onto a strain-controlled rheometer for a final calibration as shown in Fig. 3. After the gel has cured, the sample is sealed with epoxy. The sacrificial mold is then dissolved and the exposed gel is functionalized with a self-assembled polyelectrolyte multilayer to promote short-ranged adhesion and ensure no-slip boundary condition within the bilayer [24,25]. Finally, a colloidal dispersion is centrifuged to form a colloidal glass atop the substrate. Once formed, the shear post with an attached grid is lowered into the colloidal glass to a height just within the free working distance of the objective; additional colloids sediment through holes of the grid in order to embed it within the colloidal glass.

V. DATA ANALYSIS

A. Image analysis pipeline

Accurate single-particle locating is an essential analysis tool in traction rheoscopy as stress and strain are determined from the locations and displacements of individual particles within the sample. Standard particle-locating routines based on centroid locating [26,27] are augmented with three additional analysis steps: image deconvolution [28–31], nonlinear least-squares fitting [32], and a neural network used to classify the images, at the level of individual pixels, in order to distinguish colloidal particles from dimers and other synthesis by-products [33]. These additional image analysis steps, when combined with index matching and particle synthesis, allowed imaging larger volumes over longer times. The computational cost associated with the additional analysis steps is reduced by processing small, overlapping partitions of the data in parallel. All image analysis steps are carried out with open-source software packages as implemented in Deconvolution Lab 2 (image deconvolution), ilastik (pixel classifier), and TrackPy (particle locating and nonlinear least squares refinement) [26,28,32,33]. These open-source components are integrated in a Python framework with command-line job orchestration scripts; all code is freely available [34].

Development of the pipeline was motivated by an important trade-off between particle synthesis and image analysis. On the one hand, adding additional dye during particle synthesis increases the signal-to-noise ratio (SNR) of the image thereby improving the locating precision of the particles. On the other hand, adding too much dye leads to the formation of fluorescent dimers and small aggregates. Given the synthesis procedure for core-shell particles, these dimers and aggregates appear as fluorescent fused-cores with a common nonfluorescent shell and make up a small fraction of the located particles. These dimers lead to errors during particle locating in which only one of the fused cores is identified. Optimizations in particle synthesis are complemented by an image analysis pipeline that balances the trade-offs between precision and error in particle locating. To remove errors, a neural network pixel classifier is used to identify the dimers that cause errors in particle locating, and tag these located positions so that they can be removed from subsequent data analysis. Image deconvolution is used to further improve the SNR of the image. This allows reducing the laser power during image acquisition thereby extends the number of frames that can be imaged before the SNR is eventually degraded by photobleaching.

Deconvolution is applied upstream of centroid locating. Nonlinear least-squares fitting, applied downstream of the centroid locating, refines the particle positions in three dimensions and quantifies the uncertainty in each particle position. Independent of particle locating, the neural network pixel classifier is used to retain information about the fluorescence image that is otherwise obscured by particle locating. The additional information that is retained and captured by the pixel classification can be used to check for errors after the particle locating is complete. An illustrative example is the identification and removal of fused cores, which, using the method detailed in Ref. [35], were found to make up ∼1.5% of the particles located.

These image analysis tools come at an increased computational cost which is compounded by the volume of data acquired. With Nyquist sampling in all dimensions, a single stack comprising the top 30 μm of the soft gel and 100 μm shear gap consists of ∼1000 slices, corresponding to 8.8 Gb. To ensure accurate particle tracking, the shear deformation is spread out over 20–200 frames, depending on the total applied strain. As a result of the synergistic optimizations in particle synthesis and image analysis, an SNR sufficient for particle locating is maintained across the hundreds of frames that are acquired during the extended deformation. The total data size is several Tbs.

While total data size is large and the image analysis routines are computationally expensive, each small section of the data can be processed independently. To take advantage of this, the image data are split into partitions with spatial overlaps of at least one particle diameter. Each partition has dimensions $(t, z, y, x) = (1, 250, 450, 450)$ pixels with the size set to limit the peak memory usage to below 16 Gb/partition. Within each partition, the steps in the pipeline are processed serially. The small partition size, and corresponding modest memory overhead, takes advantage of the cheapest and most readily available computation blocks on high performance computing clusters.

B. Image segmentation and coordinate systems

The image analysis and particle locating pipeline segments the bilayer and separately locates the tracer particles in the silicone gel and the colloidal particles that make up the colloidal glass. Distinct coordinate systems are established in which the height of the gel tracers, $\tilde{h}$, is measured relative to the coverslip, while the height of the colloids within the colloidal glass, h, is measured relative to the top surface of the gel. Using these coordinate systems, the stress can be determined from the calibrated modulus of the silicone gel and the height-dependent displacement of the tracers embedded in the gel. Independently of the stress measurement, the strain in the sample can be determined from either the height-dependent displacement of thin layer of particles at a fixed height in the colloidal solid above the gel, or a volume average of the local best-fit affine strain measured from each particle and its shell of nearest neighbors [36]. The independent measurement of stress and strain is the central feature of this new technique. The associated uncertainties are fundamental quantities in determining the microscopic response of the colloidal solid and are detailed below.

C. Stress

We fit the positions of the first layer of particles in the colloidal glass to identify the position of the interface. The z position of the interface is used to quantify and remove axial drift in the sample. Additionally, the heights of the tracer particles above the coverslip are determined from their positions relative to this fitted plane and the measured thickness of the gel. From these positions, we fit the displacements of the tracers as function of height above the coverslip using ordinary linear least-squares regression. The slope parameter is equal to the average engineering strain, $\tilde{\gamma}_{xz}$ in the gel. For a gel of modulus of 4.9 Pa and thickness of 143 μm, a 1 μm displacement at the top surface of the gel corresponds to an engineering strain of 0.7% and shear stress of 34 mPa. In this regime, the deformation of the silicone gel is small, and its response is linear elastic. By contrast, at flow stresses of 30–40 mPa, the colloidal glass is plastically deformed.

The intercept is an open parameter in the regression and is used to rule out lateral drift. Drift measurements using the position of the interface and values of the intercepts, corresponding to axial and lateral drift, are shown in the Supplemental Material [35]. Using the measured engineering strain and calibrated modulus $\tilde{G}$, the average stress is determined: $\sigma_{xz} = \tilde{G}\tilde{\gamma}_{xz}$.

The uncertainty in the stress is evaluated from the uncertainty in the fit parameters and by examining the fit residuals.

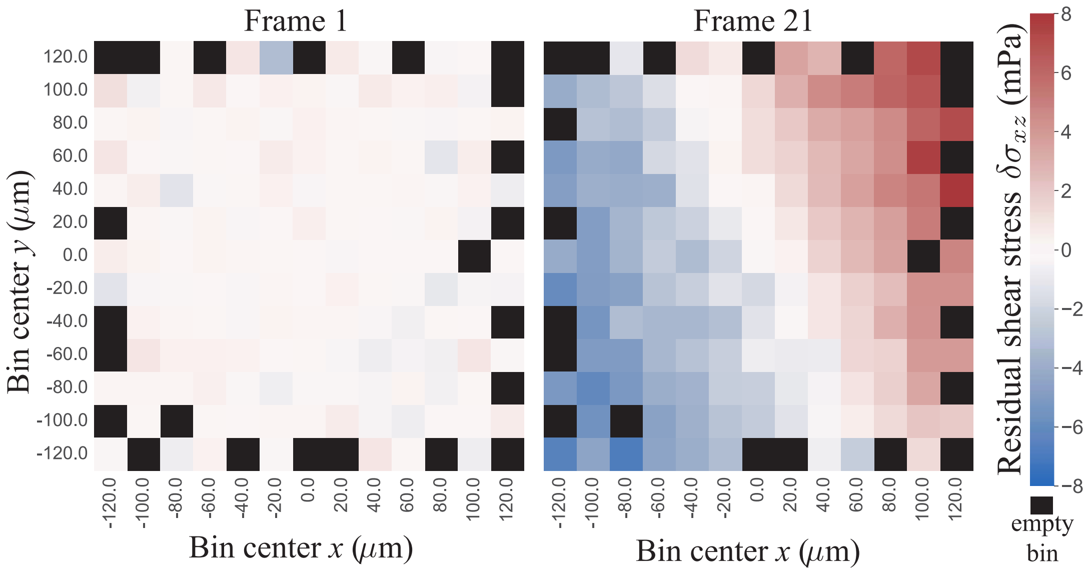

FIG. 4. Spatially resolved lateral stress variation. The average stress variation is determined from the residual displacements of tracers in the gel relative to the best fit linear regression. For each residual displacement an associated stress is calculated, and then binned laterally. Each bin contains on average four or five particles; bins that do not contain particles are shown in black. During the initial deformation between frames 1 and 3, no spatial variation in the average residuals is seen. Starting at frame 4, a smoothly varying gradient develops. This spatial variation is, at peak, ±8 mPa across the measured area, which is measurably larger than the uncertainty in stress measurements from single-particle displacements, but the gradient is less than 0.05 mPa/μm.

From the linear regression of the tracer displacement, the residual displacement for each particle is computed. This residual displacement is divided by the height of the particle, $\tilde{h}$, to obtain the residual strain, from which a residual stress is computed by multiplying by the calibrated modulus of the gel. The residual stress is binned in the xy plane, where each bin is 20 μm across and contains four or five particles on average. At the early times (frames 1–3), the uncertainty in the slope of the linear regression is constant, and the corresponding stress uncertainty is 0.8 mPa. The magnitude of this uncertainty is consistent with the uncertainty derived from the locating precision (≈25 nm) of individual tracers in the gel and the corresponding residual displacements show no spatial correlation during this time [Fig. 4(a)]. At later times, a smoothly varying spatial gradient develops across the sample. The magnitude of the gradient is maximum at the peak applied strain shown in Fig. 4(b); the magnitude increases smoothly during loading, followed by a smooth decrease during unloading.

D. Strain

The mesoscopic strain in the sample is measured in two independent ways: a boundary strain $\gamma_{xz}(h)$ is computed from the displacement of the particles at height h relative to particles at the bottom of the sediment at height $h = 0$, and a volume average of the local strain components $2\langle\epsilon_{xz}\rangle_h$. The boundary strain is $\gamma_{xz}(h) = (\langle u\rangle_h - \langle u\rangle_0)/h$, where the cumulative displacement of a particle in the shear direction $u = u(t) - u(0)$ is computed for all particles within a thin slice at height h and then averaged to obtain $\langle u\rangle$.

To complement the boundary strain measurements, we compute the local strain for each particle using a polar decomposition of the best fit linear affine deformation gradient tensor [36,37]. The affine fits for each particle are made from the relative displacements of its neighbors located within a distance less than the first minimum in the radial distribution function located at $r = 2.2$ μm. We average individual components of the strain tensor over all particles below height h to define the average local strain, $2\langle\epsilon_{xz}\rangle_h$, and compare it to the analogous boundary strain $\gamma_{xz}(h)$ computed at the same height.

From the local strain tensor measured for each particle [37], we compute a positive scalar measure of the local shear strain, known as the von Mises strain $\epsilon_{\rm vM}$:

$$\epsilon_{\rm vM} = \left[\epsilon_{xy}^2 + \epsilon_{xz}^2 + \epsilon_{yz}^2 + 1/6\big((\epsilon_{xx}-\epsilon_{yy})^2 + (\epsilon_{yy}-\epsilon_{zz})^2 + (\epsilon_{zz}-\epsilon_{xx})^2\big)\right]^{1/2}. \tag{4}$$

E. Local strain uncertainties

In contrast to the macroscopic and sample-averaged values, individual local strain measurements are limited by the locating resolution. The local strain measures the fractional change in separation distance between the particles. At close packing, this separation distance, $d = 2$ μm, is the particle diameter. The fractional change in separation distance, $\sqrt{2}\delta/d$, is determined by the locating resolution $\delta \approx 30$ nm for each of the two particles. The spread in local strain, due solely to locating uncertainties, is the uncertainty in the mean for fractional changes in separation distance (i.e., apparent strain) between particle and its neighbor:

$$\delta\epsilon \approx \frac{1}{\sqrt{N}}\frac{1}{2}\frac{\sqrt{2}\delta}{d} \approx 0.3\%, \tag{5}$$

where $1/\sqrt{N}$ accounts for the reduction in the uncertainty in the mean by including $N \approx 13$ nearest neighbors in the first coordination shell.

From this analysis, we see that that individual strain measurements have a measurement uncertainty of 0.3%, which is larger than the average shear strain applied between imaging frames. By contrast, both the volume average of the local strain tensor, $\langle\epsilon_{xz}\rangle$ and the boundary strain, γ_{xz}, can resolve shifts in the mean below 0.1%. These values should be compared to the average shear strain applied between successive imaging frames of 0.1%. This resolution has important implications for the study of shear transformation zones (STZs), which are small regions of particles that mediate plastic flow in glasses [3,4,36,38–40]. A single STZ is characterized by its volume of the central core Ω, transformation strain in the core ϵ_T, and the surrounding anisotropic elastic strain fields produced by the transformation ϵ_E, which are an order of magnitude smaller than that transformation strains, $\epsilon_E \approx \epsilon_T/10$. As an example, we consider an STZ with a small core composed of a single particle and its coordination shell that undergoes a pure shear transformation of a few percent strain ($\epsilon_T = 5\%$), and produces anisotropic elastic fields that are an order of magnitude smaller. Using these values, the transformation strain in the small core region could be resolved with single-particle strain measurements:

$$\delta\epsilon_{xz} \approx 0.3\% < \epsilon_T \approx 5\%.$$

The magnitude of the anisotropic local strain field, even close to the core where it is largest, however, is similar in magnitude to the locating resolution. We estimate that to resolve this small anisotropic strain with high spatial resolution requires an uncertainty in local strain that is an order of magnitude smaller than ϵ_E. The reduction in statistical uncertainty can, in principle, be achieved by averaging the strain fields surrounding $N \approx 100$ transformations with a similar core size and approximate transformation strain:

$$\frac{\delta\epsilon}{\sqrt{N}} = 0.3\%/10 \ll 0.5\% \approx \epsilon_E.$$

VI. MECHANICAL RESPONSE OF HARD-SPHERE COLLOIDAL GLASS

A. Spatial strain variations

Relating the internal deformation of the solid to the measured mechanical response is the central goal of combining confocal microscopy and rheology. We characterize the internal deformation of the solid using the complementary strain measures of boundary strain γ_{xz} and volume average local strain $2\langle\epsilon_{xz}\rangle_h$. We find close agreement between the strain measures for $h < 60$ µm, over all applied strains as shown in Fig. 5. This close match indicates that the local strain tensor accurately captures macroscopic strain in the sample; either strain measure can be determined with resolution below 0.1%, which is less than the incremental strain applied between frames. Consistent with direct measurements of the no-slip boundary condition, the agreement between the strains also rules out interfacial slip: a rigid body displacement of the one of the boundaries would have significant spurious effects on boundary strain but have no effect on local strain measured for particles outside the slipped region.

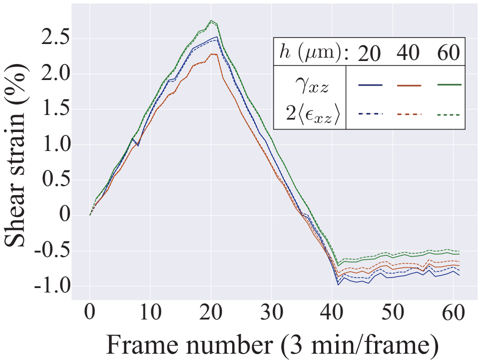

FIG. 5. Strain comparison at a selection of heights as a function of time. The macroscopic shear strain is computed in two independent ways, and shows good agreement for heights excluding the strain-localized region at the top.

Consistent with these average strain measures, we observe strain heterogeneities on multiple length scales throughout the sample. The top of the sample consists of a metal grid embedded into the colloidal glass. Just below the grid, we observe a thin, laterally extended region of high shear strain with a spatial pattern matching the grid; the the particles near the edges of the grid are highly strained over the course of the deformation. The local shear strain is quantified using ϵ_{vM} which captures this gridlike pattern as shown in Fig. 6(a). This region extends 20 µm into the sample, corresponding to a heights within the range $h = 60$–80 µm. In this region, there is inhomogeneous and localized flow corresponding to the bending of the displacement profiles shown in Fig. 2(b). This portion of the sample is excluded from volume averages of strain components. Below this inhomogeneous layer, $h < 60$ µm, we see heterogeneity of the von Mises strain at a finer scale as shown in Fig. 6(b). Additionally, we see a slightly higher average shear strain, +0.1%, at the bottom of the sample than in the middle, indicating a small but neverthe-

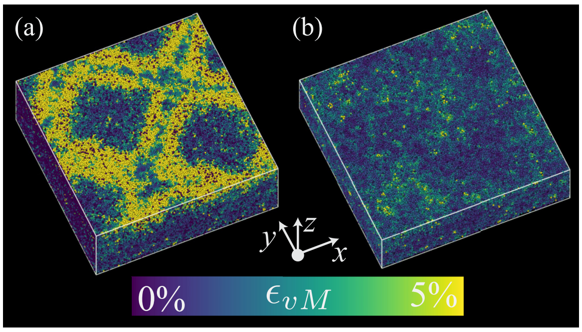

FIG. 6. Distribution and spatial heterogeneity of the local strain. The local strain is measured between frames 0 and 5. A perspective view of the full sample (a) shows the presence of a thin, laterally extended region of high von Mises strain, ϵ_{vM}, at the top of the sample with a spatial pattern that outlines the grid used to apply the deformation. Below a height of 60 µm, ϵ_{vM} local strain heterogeneities are present and distributed at a finer scale.

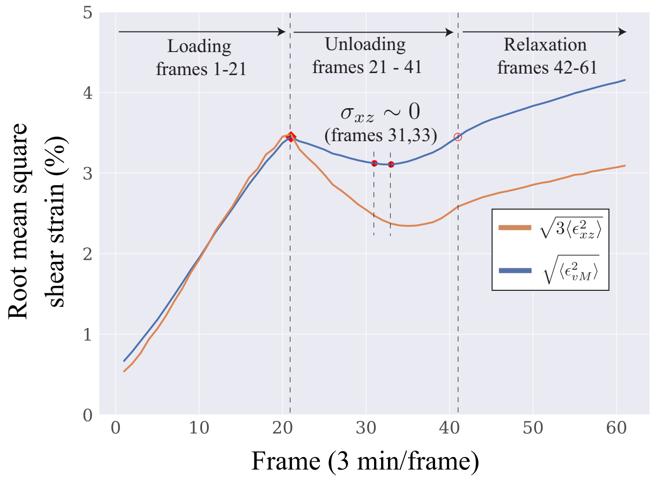

FIG. 7. Time evolution of the root-mean-square variation of shear strain components. The root mean square (RMS) of the von Mises shear strain $\epsilon_{\rm vM}$ and shear strain component, ϵ_{xz}, parallel to externally applied deformation is plotted as function of time. The peak deformation occurs at frame 21, indicated by the red diamond. As the sample is unloaded, the RMS shear strain shows a minimum near the point of zero stress (frames 31 and 33) as measured from the stress-strain curve.

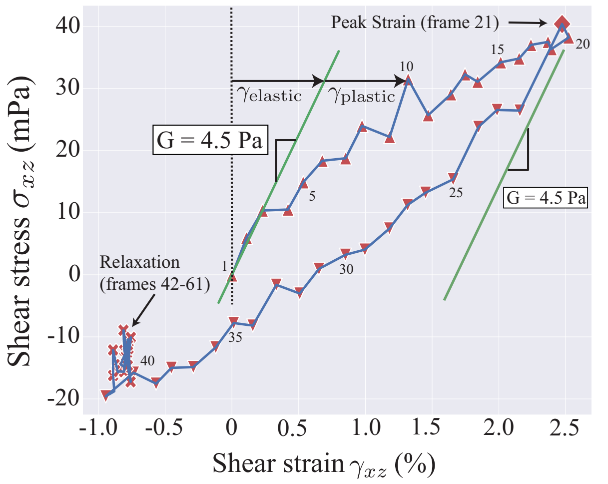

FIG. 8. Stress-strain curve. The shear modulus, G, is determined from the slope of the stress-strain curve. The stress-strain curve is further decomposed into elastic, $\gamma_{\rm elastic}$, and plastic, $\gamma_{\rm plastic}$. To compare the unloading with that of the loading part, we subtract the measured stress when the applied deformation is reversed and use that configuration as the reference configuration for the strain calculation. The loading and unloading curves show identical shear moduli up to $\gamma_{xz} \approx 0.4\%$.

less measurable mesoscopic strain variation in the bulk of the sample as shown in Fig. 5.

To assess the time evolution and heterogeneity of the local shear strain response, we compute the root mean square of the von Mises strain, $\sqrt{3\langle\epsilon_{\rm vM}^2\rangle}$, and of the shear strain component $\sqrt{\langle\epsilon_{xz}^2\rangle}$. During loading, $\sqrt{3\langle\epsilon_{\rm vM}^2\rangle}$ reaches a peak value of 3.5%, as shown in Fig. 7. During unloading, it decreases and exhibits a local minimum at frame 33, before increasing upon additional unloading. The local minimum coincides with the zero-stress crossover: the average shear stress is 0.9 mPa and −1.6 mPa at frames 31 and 33, respectively. A similar response is seen for the shear strain component ϵ_{xz}, consistent with previous observations that unloading begins with the recovery of stored elastic strain, which constitutes only a portion of the total strain [4]. This recovery continues until the sample is at zero stress and nonzero residual shear strain after which the additional applied deformation is accommodated plastically.

B. Stress-strain curve

To measure the mechanical response, we apply the stress and strain analyses to each stage of the cyclic deformation and determine the stress-strain curve shown in Fig. 8. The initial slope of the stress-strain curve, measured between frames 1 and 3, corresponds to the elastic shear modulus. Its value, 4.5 Pa, is consistent with estimates of the elastic moduli from the osmotic pressure in the sediment [35]. The macroscopic strain levels off at $\gamma_{xz} \sim 2.5\%$, which corresponds to $\sigma_{xz} \sim 40$ mPa; most of the additional deformation occurs in the inhomogeneous region near the shear post.

From the stress-strain relation, we compute the elastic and plastic response by projecting the measured stress onto an extrapolation of the initial linear portion of the stress-strain curve; the elastic strain, $\gamma_{\rm elastic}$, is the strain we expect if the material was an ideal linear elastic body with the measured shear modulus. The additional strain experienced by the material is termed the plastic strain, $\gamma_{\rm plastic}$. As the material undergoes plastic deformation, the stress begins to saturate resulting in a concomitant plateau in the elastic strain. Significant plastic strain starts to develop at total strains of only 0.3%.

The material is cyclically loaded allowing a comparison of the stress-strain relation on loading and unloading. To determine the stress on unloading, we compute the change in the stress relative to the peak stress obtained when the applied deformation is reversed at frame 21. Likewise, we compute the strain on unloading by setting the configuration at frame 21 as the reference from which the subsequent deformation is computed. After accounting for the sign change of the stress and strain, we plot the stress-strain curves for loading and unloading, and find a common elastic modulus of 4.5 Pa for both loading and unloading portions of the deformation. As a function of time, the elastic strain saturates at $\gamma_{\rm elastic} \sim 1\%$, with larger values on unloading; the plastic strain, by contrast, continues to increase, as shown in Fig. 9.

C. Micro-yielding

We develop a microscopic yielding criterion to link the locally heterogeneous response in the sample to the elastic-plastic decomposition of the macroscopic stress-strain curve. The local strain tensors are grouped based on values of the von Mises tensor invariant into *subyield* ($\epsilon_{\rm vM} < 1.5\%$) and *yielded* ($\epsilon_{\rm vM} > 1.5\%$) partitions. The threshold von Mises

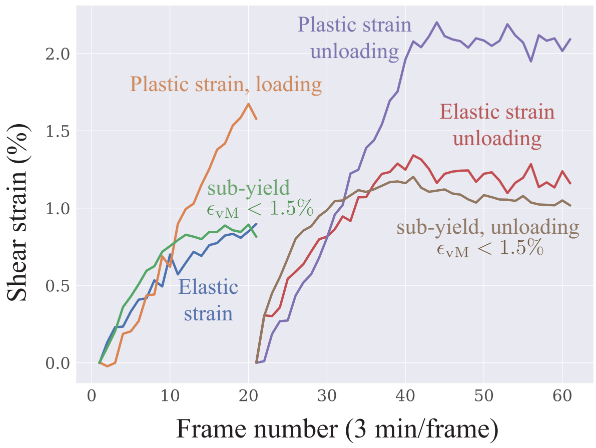

FIG. 9. Time evolution of the elastic and plastic loading. The elastic and plastic portions of the deformation are plotted as function of time for loading and unloading portions separately. A threshold von Mises strain of $\epsilon^*_{\mathrm{vM}} = 1.5\%$, partitions the local strains into *yield* and *subyield*) distributions. The average of ϵ_{xz} over the subyield distribution reproduces the macroscopic elastic strain during both loading and unloading.

strain, $\epsilon^*_{\mathrm{vM}} = 1.5\%$, is an open parameter chosen so that the time evolution of the shifts in the mean strain of the subyield partition quantitatively match the macroscopic elastic strain obtained from a decomposition of the stress-strain curve.

Using this yielding criterion to partition the particles, the distributions of tensor shear components within each partition are analyzed and compared to the corresponding macroscopic strain. In the the applied strain direction, ϵ_{xz}, the mean of the subyield distribution increases with increasing applied deformation while in the perpendicular direction, ϵ_{yz}, the mean is zero. Given the threshold von Mises strain of $\epsilon^* = 1.5\%$, the shifts in the mean in the subyield partition match the macroscopic elastic strain as shown in Fig. 9. The standard deviation, σ_{STD}, and mean, μ, of the distribution are obtained either by fitting to a normal distribution $\mathcal{N}(\mu, \sigma_{\mathrm{STD}})$, or computing the sample standard deviation and mean. In either case, the standard deviation, $\sigma_{\mathrm{STD}} \approx 0.4\%$, is similar in magnitude to the uncertainty in strain, $\delta\epsilon \approx 0.3\%$, obtained from locating uncertainties in Eq. (5) as shown in Fig. 10.

In the shear direction, the distribution over the yielded partition is skewed in the direction of applied strain and, surprisingly, contains both positive and negative values as shown in Fig. 10. Perpendicular to the shear direction, the distribution over the yielded partition remains symmetric and centered at zero as no net strain is applied in this direction. Interestingly, the yielded distribution broadens as the applied strain is increased indicative of microscopic yielding, despite there being no net strain applied in this direction.

To visualize the spatial distribution of the yielded partition, a smaller subset, constituting of only 2% of the sample, is constructed using the more stringent threshold of $\epsilon_{\mathrm{vM}} > 2.0\%$ and applying spatial clustering with size range of 5–50 particles. The resulting clusters are located throughout the sample as shown Fig. 11(a). The corresponding distribution of strains over this subset is strongly skewed in the shear direction but, similar to the yielded partition, contains both positive and negative values as shown in Fig. 11(b).

VII. CONCLUSION

In conclusion, we introduced a technique, traction rheoscopy, to carry out mechanical testing of colloidal solids that combines mPa stress resolution with single-particle visualization. The technique was demonstrated on a hard-sphere colloidal glass using compliant silicone gel as a calibrated substrate. The stress-strain curve of colloidal glass was measured, and the macroscopic mechanical response was

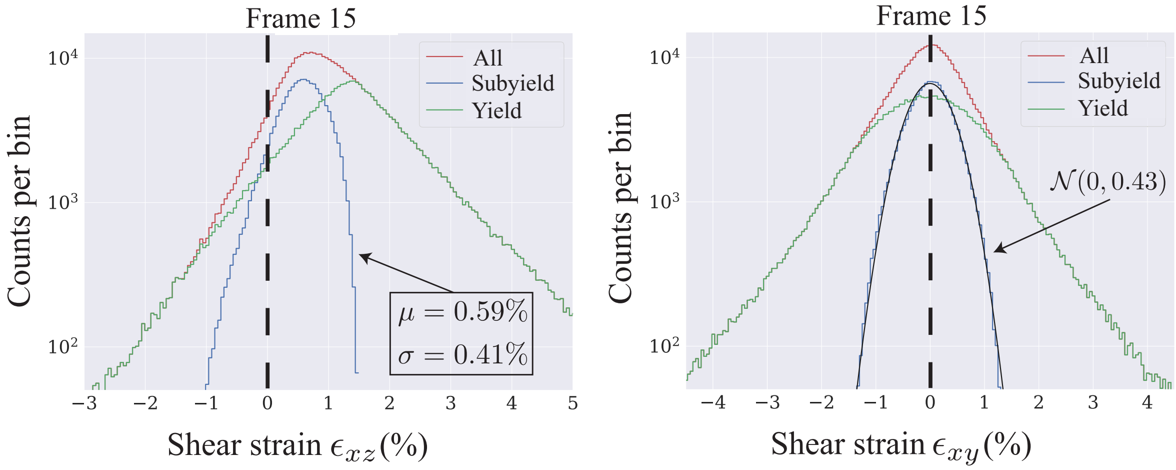

FIG. 10. Distribution of the shear strain components. The local strain components ϵ_{xz} and ϵ_{yz} are, respectively, parallel and perpendicular to the applied deformation. The full distributions (red) are partitioned into yield (green) and subyield (blue) distributions by their local von Mises shear strain, $\epsilon^*_{\mathrm{vm}} = 1.5\%$. The subyield distribution of ϵ_{yz} is normally distributed with mean 0 and standard deviation of 0.43%. The analogous distribution in ϵ_{xz} is asymmetric with a shifted mean, $\mu = 0.59\%$, in the direction of the applied deformation. The standard deviation $\sigma_{\mathrm{STD}} = 0.41\%$, computed over the subyield distribution is similar to the standard deviation of the normally distributed component, $\sigma_{\mathrm{STD}} = 0.43\%$, and consistent with the expected spread in shear strain due to locating precision.

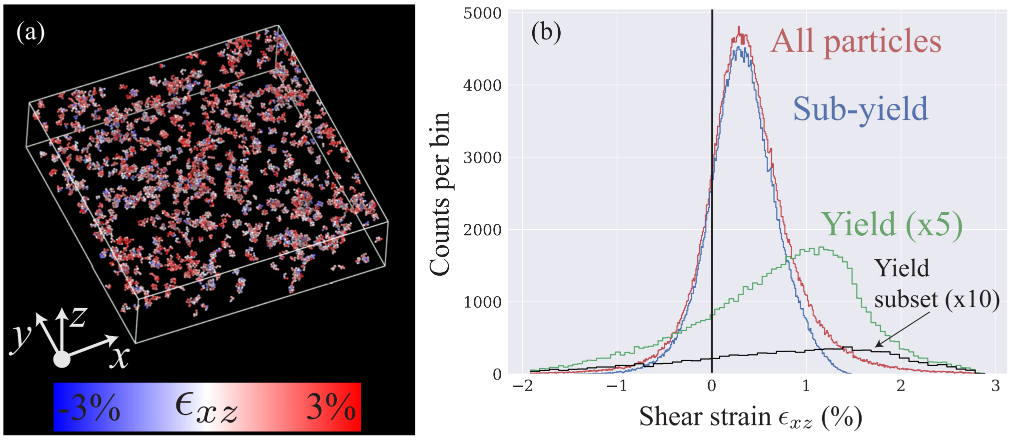

FIG. 11. Distribution and spatial heterogeneity of the local strain. The local strain is measured between frames 0 and 5. The local strain is separated into subyield ($\epsilon_{\mathrm{vM}} < 1.5\%$) and yielded ($\epsilon_{\mathrm{vM}} > 1.5\%$) partitions. A subset of yielded particles ($\epsilon_{\mathrm{vM}} > 2.0\%$), making up only 2% of the sample, is visualized in (a). The distribution of shear strains ϵ_{xz} is plotted in (b); the bin widths for yield and yield subset have been scaled by 5 and 10, respectively. The subyield distribution shows a shift in the mean, while the yielded distribution corresponds to the tails in the overall distribution.

decomposed into elastic and plastic portions. To complement the macroscopic measurement, local strain tensors were computed and were shown to be spatially heterogeneous; when averaged the local strain measurements reproduce the macroscopic strains in the sample. A microscopic yield criterion was proposed, and its relationship to macroscopic mechanical response was examined. Extension of traction rheoscopy to colloidal crystals and gels can also be achieved with the specific materials and techniques presented here. The combination of single-particle resolution and mPa stress resolution will elucidate diverse microscopic mechanisms underlying the mechanical response of colloidal solids.

ACKNOWLEDGMENTS

J.Z.T. acknowledges Emily Padston, Rodrigo Guerra, Adrian Pegoraro, and Zach Gault for fruitful discussions. This work was supported primarily by the Harvard MRSEC program of the National Science Foundation under Award No. DMR 20-11754.

---

[1] E. R. Weeks, J. C. Crocker, A. C. Levitt, A. Schofield, and D. A. Weitz, Three-dimensional direct imaging of structural relaxation near the colloidal glass transition, Science **287**, 627 (2000).

[2] P. Schall, I. Cohen, D. A. Weitz, and F. Spaepen, Visualization of dislocation dynamics in colloidal crystals, Science **305**, 1944 (2004).

[3] P. Schall, D. A. Weitz, and F. Spaepen, Structural rearrangements that govern flow in colloidal glasses, Science **318**, 1895 (2007).

[4] K. E. Jensen, D. A. Weitz, and F. Spaepen, Local shear transformations in deformed and quiescent hard-sphere colloidal glasses, Phys. Rev. E **90**, 042305 (2014).

[5] H. M. Lindsay and P. M. Chaikin, Elastic properties of colloidal crystals and glasses, J. Chem. Phys. **76**, 3774 (1982).

[6] S. K. Dutta, A. Mbi, R. C. Arevalo, and D. L. Blair, Development of a confocal rheometer for soft and biological materials, Rev. Sci. Instrum. **84**, 063702 (2013).

[7] N. Y. C. Lin, J. H. McCoy, X. Cheng, B. Leahy, J. N. Israelachvili, and I. Cohen, A multi-axis confocal rheoscope for studying shear flow of structured fluids, Rev. Sci. Instrum. **85**, 033905 (2014).

[8] R. Besseling, L. Isa, E. R. Weeks, and W. C. K. Poon, Quantitative imaging of colloidal flows, Adv. Colloid Interface Sci. **146**, 1 (2009).

[9] N. Koumakis, E. Moghimi, R. Besseling, W. C. K. Poon, J. F. Brady, and G. Petekidis, Tuning colloidal gels by shear, Soft Matter **11**, 4640 (2015).

[10] K.-H. Tran-Ba, D. J. Lee, J. Zhu, K. Paeng, and L. J. Kaufman, Confocal rheology probes the structure and mechanics of collagen through the sol-gel transition, Biophys. J. **113**, 1882 (2017).

[11] R. C. Arevalo, P. Kumar, J. S. Urbach, and D. L. Blair, Stress heterogeneities in sheared type-i collagen networks revealed by boundary stress microscopy, PLoS ONE **10**, e0118021 (2015).

[12] V. Rathee, D. L. Blair, and J. S. Urbach, Localized stress fluctuations drive shear thickening in dense suspensions, Proc. Natl. Acad. Sci. USA **114**, 8740 (2017).

[13] A. Egner and S. W. Hell, Aberrations in confocal and multiphoton fluorescence microscopy induced by refractive index mismatch, in *Handbook of Biological Confocal Microscopy*, edited by J. B. Pawley (Springer US, Boston, 2006), pp. 404–413.

[14] S. Hell, G. Reiner, C. Cremer, and E. H. Stelzer, Aberrations in confocal fluorescence microscopy induced by mismatches in refractive index, J. Microsc. **169**, 391 (1993).

[15] N. Martini, J. Bewersdorf, and S. W. Hell, A new high-aperture glycerol immersion objective lens and its application to 3D-fluorescence microscopy, J. Microsc. **206**, 146 (2002).

[16] J. Z. Terdik, D. A. Weitz, and F. Spaepen, Ultrasoft silicone gels with tunable refractive index for traction force microscopy, Soft Matter **20**, 4633 (2024).

[17] T. E. Kodger, R. E. Guerra, and J. Sprakel, Precise colloids with tunable interactions for confocal microscopy, Sci. Rep. **5**, 14635 (2015).

[18] J. C. Scanlan and H. H. Winter, Composition dependence of the viscoelasticity of end-linked poly(dimethylsiloxane) at the gel point, Macromolecules **24**, 47 (1991).

[19] M. Kogan, C. J. Dibble, R. E. Rogers, and M. J. Solomon, Viscous solvent colloidal system for direct visualization of suspension structure, dynamics and rheology, J. Colloid Interface Sci. **318**, 252 (2008).

[20] P. J. Flory, *Principles of Polymer Chemistry* (Cornell University Press, Ithaca, NY, 1953).

[21] J. Z. Terdik, D. A. Weitz, and F. Spaepen, Fabrication and mounting of near-critical silicone gels for mechanical testing of colloidal solids (unpublished).

[22] E. R. Jerison, Y. Xu, L. A. Wilen, and E. R. Dufresne, Deformation of an elastic substrate by a three-phase contact line, Phys. Rev. Lett. **106**, 186103 (2011).

[23] S. Mora, T. Phou, J.-M. Fromental, L. M. Pismen, and Y. Pomeau, Capillarity driven instability of a soft solid, Phys. Rev. Lett. **105**, 214301 (2010).

[24] P. T. Hammond and G. M. Whitesides, Formation of polymer microstructures by selective deposition of polyion multilayers using patterned self-assembled monolayers as a template, Macromolecules **28**, 7569 (1995).

[25] M. Schönhoff, Self-assembled polyelectrolyte multilayers, Curr. Opin. Colloid Interface Sci. **8**, 86 (2003).

[26] D. Allan, T. Caswell, N. Keim, C. M. van der Wel, and R. Verweij, *Soft-matter/trackpy: Trackpy*, ver. 0.5.0 (Zenodo, Geneva, 2021).

[27] J. C. Crocker and D. G. Grier, Methods of digital video microscopy for colloidal studies, J. Colloid Interface Sci. **179**, 298 (1996).

[28] D. Sage, L. Donati, F. Soulez, D. Fortun, G. Schmit, A. Seitz, R. Guiet, C. Vonesch, and M. Unser, Deconvolutionlab2: An open-source software for deconvolution microscopy, Methods **115**, 28 (2017).

[29] L. B. Lucy, An iterative technique for the rectification of observed distributions, Astron. J. **79**, 745 (1974).

[30] W. H. Richardson, Bayesian-based iterative method of image restoration, J. Optical Soc. America **62**, 55 (1972).

[31] N. Dey, L. Blanc-Feraud, C. Zimmer, P. Roux, Z. Kam, J.-C. Olivo-Marin, and J. Zerubia, Richardson–Lucy algorithm with total variation regularization for 3D confocal microscope deconvolution, Microscopy Res. Tech. **69**, 260 (2006).

[32] C. van der Wel and D. J. Kraft, Automated tracking of colloidal clusters with sub-pixel accuracy and precision, J. Phys.: Condens. Matter **29**, 044001 (2017).

[33] C. Sommer, C. Straehle, U. Köthe, and F. A. Hamprecht, Ilastik: Interactive learning and segmentation toolkit, in *Proceedings of the 2011 IEEE International Symposium on Biomedical Imaging: From Nano to Macro* (IEEE, Piscataway, NJ, 2011), pp. 230–233.

[34] https://github.com/tlozsolt/TractionRheoscopy.

[35] See Supplemental Material at http://link.aps.org/supplemental/10.1103/PhysRevE.110.024606, for the data analysis procedures identifying fluorescent dimers from fluorescent core-shell particles including GitHub repository at Ref. [34], and image analysis and particle locating algorithms including Refs. [26–33,41,42]; the removal of microscope drift using the displacements of the tracer particles embedded in the gel; and a calculation of the elastic moduli of hard-sphere systems near random close packing including Refs. [43–45].

[36] M. L. Falk and J. S. Langer, Dynamics of viscoplastic deformation in amorphous solids, Phys. Rev. E **57**, 7192 (1998).

[37] A. Stukowski, Visualization and analysis of atomistic simulation data with OVITO—The Open Visualization Tool, Modell. Simul. Mater. Sci. Eng. **18**, 015012 (2010).

[38] A. Argon, Plastic deformation in metallic glasses, Acta Metall. **27**, 47 (1979).

[39] F. Spaepen, A microscopic mechanism for steady state inhomogeneous flow in metallic glasses, Acta Metall. **25**, 407 (1977).

[40] J. D. Eshelby, The determination of the elastic field of an ellipsoidal inclusion, and related problems, Proc. R. Soc. London A **241**, 376 (1957).

[41] A. K. Wong and P. K. Sahoo, A gray-level threshold selection method based on maximum entropy principle, IEEE Trans. Syst. Man Cybernetics **19**, 866 (1989).

[42] K. E. Jensen and N. Nakamura, Note: An iterative algorithm to improve colloidal particle locating, Rev. Sci. Instrum. **87**, 066103 (2016).

[43] J. G. Kirkwood, Critique of the free volume theory of the liquid state, J. Chem. Phys. **18**, 380 (1950).

[44] Z. W. Salsburg and W. W. Wood, Equation of state of classical hard spheres at high density, J. Chem. Phys. **37**, 798 (1962).

[45] S. Torquato and F. H. Stillinger, Jammed hard-particle packings: From Kepler to Bernal and beyond, Rev. Mod. Phys. **82**, 2633 (2010).